Star formation and AGN activity in distant massive galaxies

Podigachoski, Pece

Chapter 5

Starbursts and dusty tori in distant 3CR radio galaxies

– **P. Podigachoski, B. Rocca-Volmerange, P. D. Barthel, G. Drouart, and M. Fioc** –

Monthly Notices of the Royal Astronomical Society, 2016, **462**, 4183

Abstract

We present a study of the complete ultraviolet to submillimetre spectral energy distributions (SEDs) of twelve 3CR radio galaxy hosts in the redshift range $1.0 < z < 2.5$, which were all detected in the far-infrared by the *Herschel Space Observatory*. The study employs the new spectro-chemical evolutionary code PÉGASE.3, in combination with recently published clumpy AGN torus models. We uncover the properties of the massive host galaxy stellar populations, the AGN torus luminosities, and the properties of the recent starbursts, which had earlier been inferred in these objects from their infrared SEDs. The PÉGASE.3 fitting yields very luminous (up to $10^{13}\,L_{\odot}$) young stellar populations with ages of several hundred million years in hosts with masses exceeding $10^{11}\,M_{\odot}$. Dust masses are seen to increase with redshift, and a surprising correlation – or better upper envelope behaviour – is found between the AGN torus luminosity and the starburst luminosity, as revealed by their associated dust components. The latter consistently exceeds the former by a constant factor, over a range of one order of magnitude in both quantities.

5.1 Introduction

The episodic accretion of matter onto supermassive black holes (SMBH), which are nowadays assumed to exist in the central regions of almost all massive galaxies in the Universe, results in phenomena known as active galactic nuclei (AGN). Because of the interaction with their host galaxies, primarily exhibited via negative and/or positive feedback processes, AGN are essential elements – or phases – in the evolution of galaxies through cosmic time. Particular attention in studies of galaxy evolution is paid to the early epoch $1 < z < 3$, which is the time when both the stellar bulges of galaxies and their associated black holes went through peak growth (Alexander & Hickox 2012; Heckman & Best 2014).

A small fraction of AGN are characterized by strong radio emission, which is produced by the powerful radio-jets and radio-lobes driven by the growth of the black hole. The most powerful radio-loud AGN are the so-called FRII sources (Fanaroff & Riley 1974). By virtue of their huge radio luminosities, these sources were historically used in searches for the most distant objects in the Universe (Roettgering et al. 1994; Stern & Spinrad 1999). While no longer being the highest redshift holders, radio-loud AGN (and their hosts) have remained central in studies of the interplay between AGN and star formation (SF) activity in massive galaxies in the early Universe (see Miley & De Breuck 2008, for a review). The reasons are straightforward: high-z radio-loud AGN are powerful AGN (Haas et al. 2008; De Breuck et al. 2010; Dicken et al. 2014), and their hosts are among the most massive galaxies in the Universe (Best et al. 1998a; Seymour et al. 2007) often showing prodigious levels of SF activity (Archibald et al. 2001; Reuland et al. 2004; Drouart et al. 2014; Tadhunter et al. 2014; Podigachoski et al. 2015b). From the sharp cut in the Hubble K-band diagram, and using elliptical scenarios corrected for evolution and cosmology, Rocca-Volmerange et al. (2004) estimated a maximum stellar mass of $10^{12}\,\mathrm{M}_{\odot}$ for $1 < z < 4$ objects.

Additionally, radio-loud AGN are often used in unification studies. Within the framework of the unified model of radio-loud AGN (Barthel 1989), FRII radio galaxies (RGs, type 2) and radio-loud quasars (type 1) are assumed to belong to the same parent population, and can be unified based on orientation (see Antonucci 2012, for a recent review). Central to this model is the AGN torus, a region rich in molecular gas and dust perpendicular to the radio source axis, obscuring the accretion disc and the broad-line region along a substantial range of viewing angles (e.g., Drouart et al. 2012). In the case of RGs, the torus acts like a natural coronograph, blocking most of the UV/optical light emitted due to the AGN activity (e.g., Wilkes et al. 2013) and – in contrast to quasars – enabling detailed studies of the stellar populations of the AGN host galaxy.

Originally selected at low radio frequencies (178 MHz), the landmark Revised Third Cambridge Catalogue of Radio Sources (hereafter 3CR; Spinrad et al. 1985) contains some of the brightest radio-loud AGN at all redshifts. The $z > 1$ double-lobed (FRII) RGs and quasars in the 3CR sample almost universally accrete at high Eddington rates, i.e. in quasar-mode (e.g., Best & Heckman 2012), resulting in an unbiased sample, free of any of the low-power AGN often found at lower redshifts ($z \sim 0.5$). The $z > 1$ part of this sample has been observed with virtually all space-based telescopes (Best et al. 1997;

Haas et al. 2008; Leipski et al. 2010; Wilkes et al. 2013; Chiaberge et al. 2015), including the *Herschel* telescope (Barthel et al. 2012; Podigachoski et al. 2015b).

Using primarily *Spitzer* and *Herschel* broad-band photometry, Podigachoski et al. (2015b) decomposed the rest-frame infrared (IR) spectral energy distributions (SEDs) of the complete $z > 1$ 3CR sample into AGN- and SF-related components, adopting for the latter a typical modified blackbody with a fixed dust emissivity index. Compared to studies of other radio-loud AGN in the high-z Universe (e.g., Drouart et al. 2014), Podigachoski et al. (2015b) found a somewhat higher *Herschel* detection fraction, with about half of their sample objects detected in at least three *Herschel* bands, indicating rates (SFRs) of several hundred solar masses per year. Such prodigious SFRs, at the level of those of typical submillimetre galaxies at similar redshifts, were found despite the powerful AGN activity which often dominates the IR luminosities of the 3CR objects, ruling out uniform quenching of star formation and providing tentative evidence for jet-triggering of star formation (Podigachoski et al. 2015b). Adopting a modified blackbody component to account for the emission of the star-formation-heated dust provides robust estimates of the temperature and the mass of this cold dust in AGN hosts; however, it yields no information on the mass, age, and/or metallicity of the (young) stellar component which powers the dust emission in the rest-frame far-infrared (FIR). Such information, particularly for AGN hosts which are not completely enshrouded by dust, can be robustly obtained by also considering the unattenuated part of the stellar continuum due to the young stars. Furthermore, by only exploring SEDs beyond 1 μm in the rest-frame of the objects, Podigachoski et al. (2015b) do not consider the evolved stellar populations in the hosts of 3CR AGN, which are expected to peak at about 1 μm in the rest-frame.

Here, we extend the work of Podigachoski et al. (2015b) by studying the rest-frame ultraviolet (UV) to submillimetre (submm) SEDs of twelve $z > 1$ 3CR RG hosts, identifying the emissions from the past and recent stellar populations and from the AGN torus, with the goal to constrain the physical properties of these stellar populations. We use the new spectro-chemical evolutionary code PÉGASE.3 (Fioc & Rocca-Volmerange, in preparation), which follows the masses of stars, gas and dust, determines the attenuation of stellar emission by grains in H II regions and the diffuse interstellar medium (ISM), and consistently computes the emission of the latter. Galaxy templates computed with PÉGASE.3 were earlier used by Rocca-Volmerange et al. (2013), who performed a pilot study of two distant ($z = 3.8$) RGs selected for their small AGN contributions. Coupling PÉGASE.3 templates with smooth torus models by Fritz et al. (2006), Drouart et al. (2016) recently extended this pilot study to a sample of 11 more powerful RGs from the $1 < z < 4$ sample of Drouart et al. (2014). Here, we use the latest torus models in the literature (Siebenmorgen et al. 2015) in a study of a dozen well-known 3CR RGs, also aiming to test the different AGN torus formalisms. We consider only RGs, but maintain the view that most results obtained for this AGN class are applicable also for radio-loud quasars within the unified model of radio-loud AGN (e.g., Podigachoski et al. 2015a).

This paper is organized as follows. In § 5.2 we present the sample used in this work, and the observational data which we use as input for our SED fitting approach. In § 5.3 we provide overview of the PÉGASE.3 model predictions including a coherent

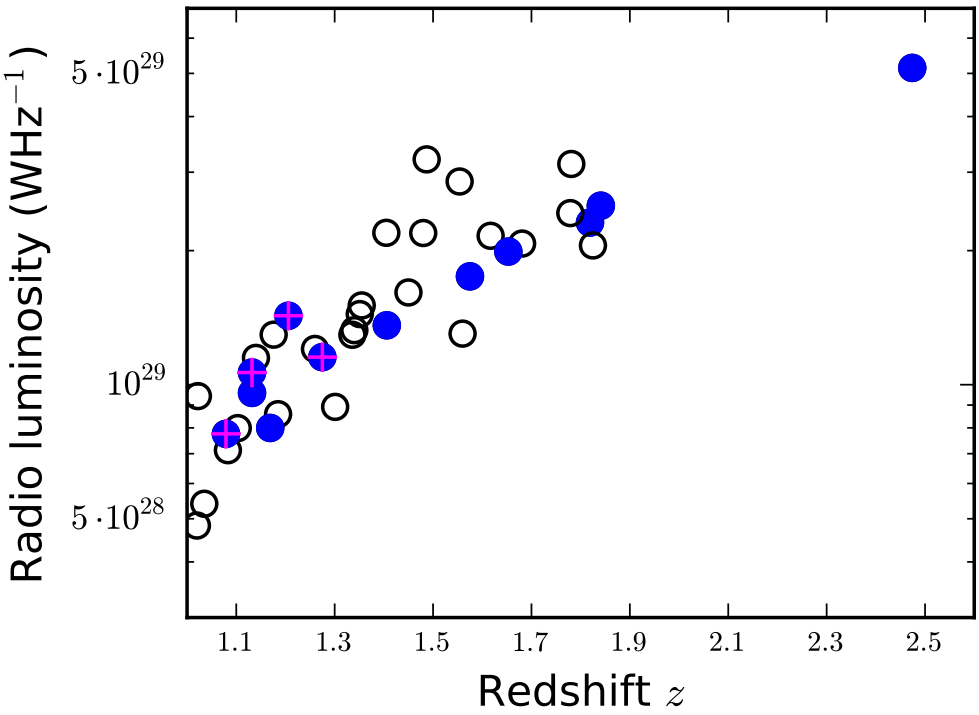

Figure 5.1: Sample selection. Plotted is the observed radio (178 MHz) luminosity as a function of redshift for the complete $z > 1$ 3CR sample of radio galaxies. The subsample of radio galaxies with good signal-to-noise detections from UV to submm wavelengths, which is the one considered in this work (see text), is shown with filled symbols. Objects belonging to this subsample for which *Spitzer* spectra are available, are indicated with crosses.

dust emission, and of the adopted library of torus models. The results, including the best-fit SEDs of each sample object, are presented in § 5.4, and discussed in § 5.5. We conclude this paper with a brief summary (§ 5.6). The Appendix contains details on the observational data for each object studied in this work.

5.2 Sample selection and data

The RGs studied in this work belong to the Third Cambridge Catalog of Radio Sources (Bennett 1962; Spinrad et al. 1985). Being selected due to their steep-spectrum radio emission from their radio-lobes, these objects are some of the most powerful AGN at any redshift in the Universe. The sample studied in this work is a subset of the complete high-z ($z > 1$) catalog of 3CR RGs, which contains a total of 37 RGs (Spinrad et al. 1985). The highest redshift object is 3C 257 at $z = 2.474$, while all other sources are at redshifts $1 < z < 2$.

Table 5.1: The twelve objects selected from the complete $z > 1$ 3CR sample of radio galaxies and studied in this work. The star symbols next to the names indicate objects for which *Spitzer* IRS spectra are available.

Name	z	$\log(L_{178\ MHz}(W\ Hz^{-1}))$
3C 068.2	1.57	29.2
3C 210	1.17	28.9
3C 256	1.82	29.4
3C 257	2.47	29.7
3C 266*	1.27	29.1
3C 297	1.41	29.1
3C 305.1	1.13	29.0
3C 324*	1.21	29.2
3C 356*	1.08	28.9
3C 368*	1.13	29.0
3C 454.1	1.84	29.4
3C 470	1.65	29.3

Decomposing the spectral energy distributions of RGs into stellar and AGN-related components requires observations at the MIR. The complete high-z 3CR sample has been observed at six different bands at wavelengths between 3.6 and 24 μm with all *Spitzer* imaging instruments (Haas et al. 2008). Given that almost all RGs have been detected with all *Spitzer* instruments at good signal-to-noise ratios, the *Spitzer* photometry does not introduce any selection effects. We note however, that such effects are introduced when selecting objects which have been detected in the rest-frame FIR and UV/optical bands, as described below.

A crucial step forward in understanding the properties of the high-z 3CR sample has recently been provided by *Herschel* imaging, using both imaging instruments (PACS at 70 and 160, and SPIRE at 250, 350, and 500 μm). Full details on the data reduction and photometry of the 3CR sample are provided by Podigachoski et al. (2015b). As shown in that paper, the typical temperature of the cold dust in 3CR hosts is about 40 K, which means that the peak due to the dust-reprocessed young stellar emission occurs at around 70 μm. To constrain this peak, we require that each RG is detected in at least one photometric band at rest-frame wavelength greater than 70 μm, which given the redshift of our RGs requires that the objects are detected in the SPIRE 250 μm band[1]. This is in fact the main criterion we impose when selecting the RGs for the current work, and this criterion is only relaxed in two cases, 3C 210 and 3C 356, because despite them being detected in only the two PACS bands, their sufficiently low redshift ensures that the PACS 160 μm band probes emission beyond the infrared peak. Fifteen RGs satisfy this selection criterion. Clearly, selecting the *Herschel*-detected RGs means that our work features only the most prodigiously star-forming 3CR RGs. However, as pointed out by

[1] Note that all objects with a robust SPIRE 250 detection are also detected in both PACS bands.

Podigachoski et al. (2015b), the objects not detected with *Herschel* might still actively form stars, though at a significantly lower level.

In addition to powering the dust-reprocessed emission in the FIR, young stars – when not attenuated – also emit strongly in the UV/optical. Furthermore, the evolved stellar populations produce stellar continuum radiation which peaks in the optical/NIR (Rocca-Volmerange et al. 2013). Both considerations render UV-to-NIR observations crucial to our SED study of RGs. A major study of the properties of $z \sim 1$ 3CR RGs was performed by Best et al. (1997), whose work is the source of most NIR data and about half of the UV/optical data used in our work[2]. More UV/optical observations with the improved *Hubble Space Telescope (HST)* were recently obtained as part of an *HST SNAPSHOT* programme (Chiaberge et al. 2015; Hilbert et al. 2016). To better constrain the ages of the stellar populations, we require that each RG has at least two photometric observations, one on either side of the 4000Å break. This selection criterion limits the 15 *Herschel*-detected objects to 13, which can be grouped as follows: 8 have at least two *HST* and one NIR observation (mainly provided by Best et al. 1997), and 5 have only two *HST* observations (mainly provided by Chiaberge et al. 2015) and no NIR observations. The prominent emission lines seen in the UV/optical spectra of high-z RGs (e.g., McCarthy 1993; Best et al. 2000a), including but not limited to C II, Ne V, O II, H β, O III and H α may have an important contribution ($\sim$30%) to the total flux measured in broadband filters; these line fluxes have been subtracted based on optical spectra as explained in the corresponding reference papers (Best et al. 1997; Hilbert et al. 2016).

Hence, the final sample studied in this work contains 12 well-known type 2 AGN of the 13 RGs which satisfy both selection criteria: we remove 3C 119 from the subsequent analysis, because it has been shown that it is an object with a quasar-like NIR/MIR SED (see Podigachoski et al. 2015a). The location of the sample in the radio luminosity-redshift plane is shown in Fig. 5.1. As shown in that figure, the selected RGs are homogeneously distributed in redshift. The main parameters of the final sample addressed in this work are summarized in Table 5.1. Tables listing the details of the available photometry used for the fitting for each of these RGs are presented in the Appendix.

In addition to the photometric observations presented above, some[3] 3CR RGs with redshifts $z < 1.4$ have been observed in spectroscopic mode with the IRS spectrograph on *Spitzer* (Leipski et al. 2010). The availability of such spectra is not a selection criterion in our work: the spectra are merely used to confirm that the torus models which we apply (see below) account well for the MIR photometry of RGs, and that the disentangling of AGN and young stellar components in the important MIR/FIR transition region is

[2] The Best et al. (1997) *Hubble Space Telescope* observations were later re-analysed by Inskip et al. (2006), who extracted the photometry of the 3CR RGs in 4″ apertures as opposed to the 9″ (diameter) apertures used by Best et al. (1997). To compute colors at the exact same filters for each RG, in most cases Inskip et al. (2006) relied on interpolations based on observations in other nearby filters. To avoid the additional uncertainty associated with this step, we choose the Best et al. (1997) measurements despite the fact that some of our objects may have some contamination from nearby objects within the larger aperture (see § 5.5.4).

[3] Leipski et al. (2010) in fact studied the complete sample of 3CRR radio-loud AGN at the redshift range $1 < z < 1.4$, but because the 3CRR catalogue is a subsample of the parent 3CR catalogue studied in this work, the few 3CR RGs in this redshift range not belonging to 3CRR do not have *Spitzer* spectroscopy.

reasonably robust. Given the spectral window covered by the IRS spectrograph, between 19.5 and 36.5 μm, and the redshift range of the 3CR RGs given above, the *Spitzer* spectra often contain both low- and high-excitation MIR emission lines (e.g., Ne II, Ne V, Ne III), the 11.3 μm line from PAH features, and the 9.7 μm silicate feature (Leipski et al. 2010). To include the spectroscopic information to the SED analysis, we measure flux densities at three artificial broadband filters centred at 27, 30, and 33 μm. The RGs which have *Spitzer* spectra are: 3C 266, 3C 324, 3C 356, and 3C 368 (see Table 5.1).

Finally, some objects from our final sample also have SCUBA/MAMBO submm (850 μm) observations. Given that our high-z 3CR RGs are exclusively steep-spectrum radio sources, any synchrotron emission from the radio lobes can safely be neglected, and in practice, these observations probe the Rayleigh-Jeans tails of the thermal dust continuum emission (see e.g., Haas et al. 2006; Podigachoski et al. 2015b).

5.3 Models and templates

The templates used in this work are built with the help of two models: the evolutionary synthesis code PÉGASE.3 (Fioc & Rocca-Volmerange, in preparation), and the AGN torus model by Siebenmorgen et al. (2015). Both models use Monte Carlo simulations for solving the radiative transfer equations.

5.3.1 Pégase.3 models

PÉGASE.3, predicts the attenuated star and gas emission, and the coherent dust emission from the attenuation, coherently transferred through the diffuse ISM and star forming regions. Built as a flexible tool, PÉGASE.3 provides an extensive range of choices in terms of star formation rates, initial mass functions, and infall or outflow rates to mimic the galaxy evolution for starbursts and various spectral types over a large redshift range. It tracks the chemical ISM enrichment of specifically the elements C and Si, plus O, Fe, N, and other metals, from which dust mass grows. At any wavelength, the code sums the contributions of the stellar photospheric emission, nebular continuum and the dust emission of the heated grains. Destruction and accretion dust phases are considered using classical Draine models and specific modelling (Dwek 1998). Through Monte Carlo simulations of radiative transfer, the attenuation (absorption and scattering) and dust re-emission (including stochastic heating) are predicted for various geometries (slab, spheroids, bulges + disks). The main difference of PÉGASE.3 with most other models is the coherence in metal enrichment from the stellar ejecta derived from the adopted star formation law. Extended to a large coverage of wavelength domain and respecting energy conservation, it is used in place of extinction laws or any UV-far-IR relations. Galaxy scenarios by type are defined with a limited number of free parameters (star formation rate, infall, outflow and initial mass function) to be compatible with the local SDSS galaxy color-color distribution (Tsalmantza et al. 2012). The detailed documentation (at `www2.iap.fr/pegase`) provides the possibility to propose new scenarios among which those derived from semi-analytic models or numerical simulations. As 3CR RG hosts are expected to be massive ellipticals occasionally undergoing bursts of star formation, we consider here only starburst and early type scenarios, as used by Rocca-Volmerange et al. (2013) and Drouart et al. (2016).

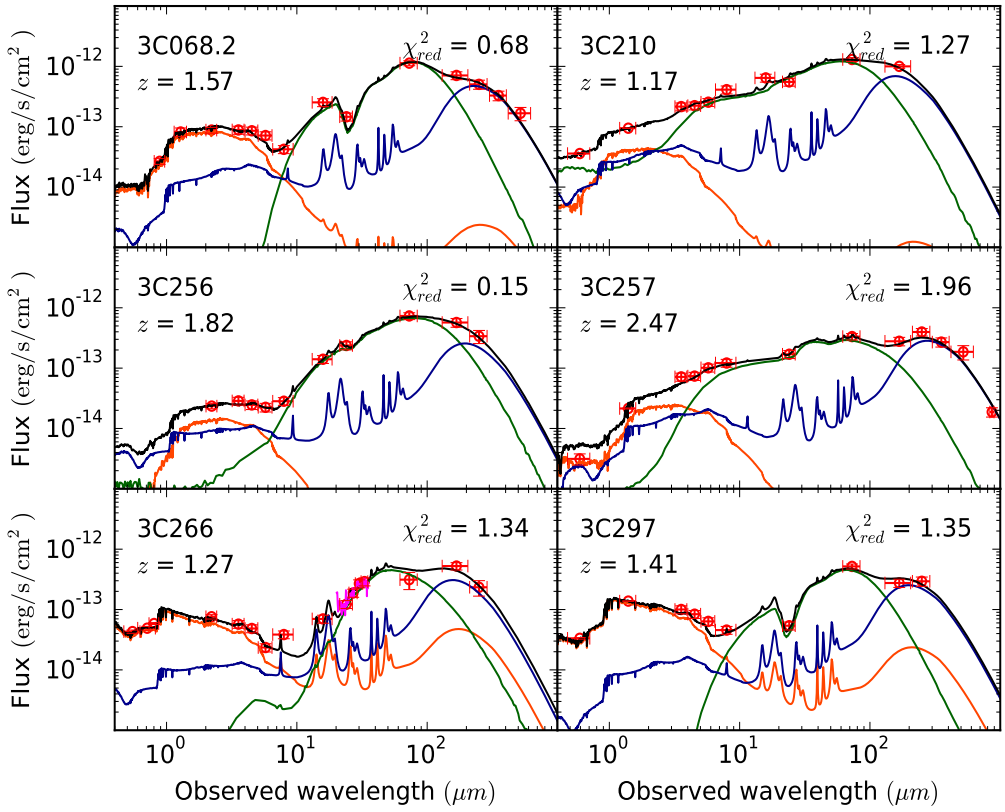

Figure 5.2: The best-fit UV-to-submm spectral energy distributions (SEDs) of the 3CR radio galaxies studied in this work. The observed SEDs (in units λF_λ) are shown with red symbols. The components combining to yield the total SED (black) are as follows: old stellar component modelled with Pégase.3 (orange), young stellar component modelled with Pégase.3 (blue), and AGN-powered torus component (green) from the library of Siebenmorgen et al. (2015). Overplotted in magenta are the *Spitzer* IRS spectroscopic observations, available for selected sources. Zoom-ins of the regions probed by these spectra are shown in Fig. 5.3.

5.3.2 AGN torus models

The high-z 3CR RGs are demonstrably powerful emitters in the rest-frame MIR (Haas et al. 2008; Podigachoski et al. 2015b), where thermal emission from the AGN torus dust is the most dominant emission process. The physical origin of and the distribution of dust within the AGN torus are hotly debated issues in the literature. The two main families of models in the literature are the smooth models (e.g., Fritz et al. 2006), whereby dust is distributed homogeneously throughout the torus, and the clumpy models (e.g., Nenkova et al. 2008; Hönig & Kishimoto 2010), whereby dust is located in individual dusty clouds filling the torus. A number of photometric and spectroscopic studies have been performed aiming to pin down the relevant physical parameters within a given for-

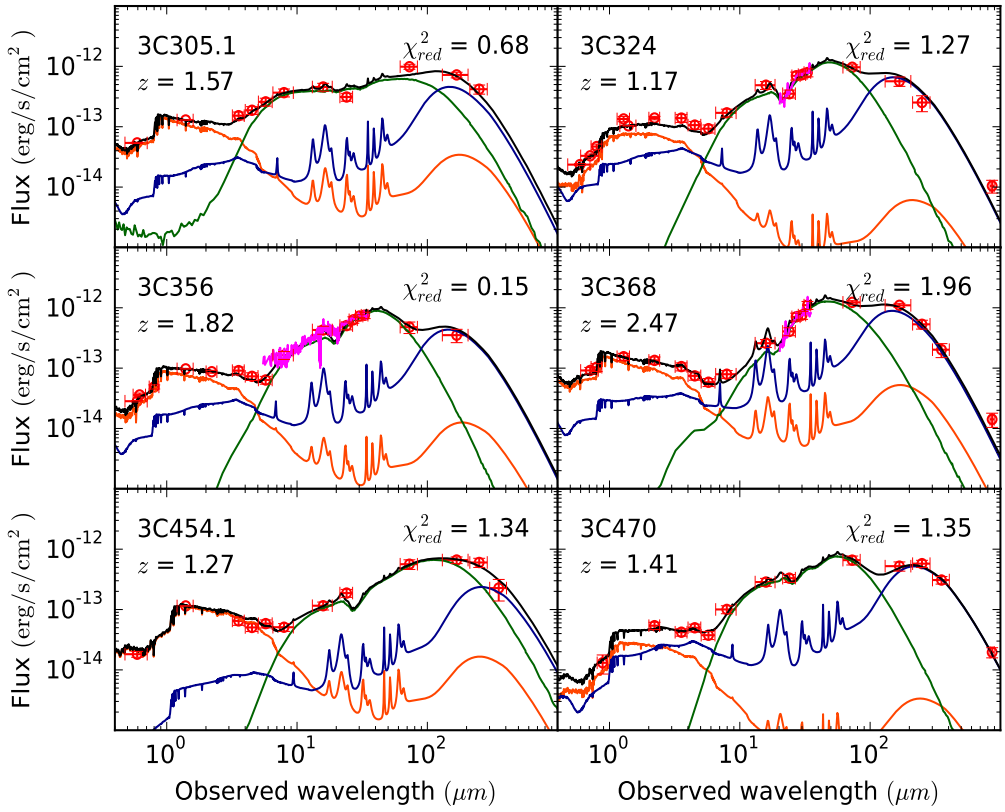

Figure 5.2: Continued.

malism, yet the best evidence (albeit from a small number of nearby objects) comes from MIR interferometric studies (e.g., Hönig et al. 2013, and references therein).

In this work, we adopt the models presented by Siebenmorgen et al. (2015), whose formalism includes both a homogeneous disc of gas and individual dust clouds randomly distributed throughout the torus. The five free parameters of these models are: (i) viewing angle (9 values), (ii) inner torus radius (5 values), (iii) volume filling factor of clouds (4 values), (iv) optical depth of clouds (4 values), and (v) optical depth of disc midplane (5 values), which results in a library of 3600 unique torus models. Given the dense environment in circumnuclear regions, the Siebenmorgen et al. (2015) models adopt fluffy dust grains, a choice resulting in stronger FIR and submm emission compared to other clumpy models, but also a more pronounced NIR emission because the larger (than standard ISM) fluffy grains can survive much closer to the AGN. This, together with the additional material in the innermost region of the torus provided by the homogeneous disc and the dust clouds in the ionization cones of the AGN naturally reproduces the NIR bump seen in some RGs. Note that given the limited photometric data in the MIR in this work, we cannot study the torus in detail, and we stress that our goal is to simply isolate the AGN-powered emission from the stellar emission.

5.3.3 SED fitting procedure

Following the approach by Drouart et al. (2016), synthetic libraries of early-type galaxy and starburst plus AGN templates are built with a variety of parameters over large ranges. The free parameters for the early-type galaxy templates include the normalization and the age of the stellar component, and the ones for the starburst templates include the initial metallicitiy in addition to the age and normalization of this stellar component. More than 10^7 templates are tested for comparison to the global observed spectral energy distributions. The instantaneous starburst (see Rocca-Volmerange et al. 2013) is preferred to test the most powerful emitters in the far-IR: its parameters are a Kroupa et al. (1993) initial mass function, and no outflow or infall. As described by Drouart et al. (2016), the AGN templates are added to each starburst template as a relative contribution at 20 μm, using a grid of values ranging between dominant to negligible AGN contribution at this particular wavelength. Observations are compared to the sum of normalized SED templates by a χ^2-minimization procedure (Le Borgne & Rocca-Volmerange 2002) on the largest wavelength coverage, providing the best-fit of the bolometric luminosity. The calibration factor is derived from the global best-fit synthetic SED compared to the observations, which is then applied to all normalized Pégase.3 outputs (e.g., masses, luminosities, etc.)

5.4 Results

In this section we discuss the overall successes and limitations of the SED fitting approach, and the results obtained from the best-fit SEDs. The best-fit SEDs are presented in Fig. 5.2 and Fig. 5.3, and details on the observations of twelve individual RG hosts are provided in the Appendix. We mainly focus on the physical properties of the young stellar component obtained from the best-fits, and the possible link between its infrared luminosity and that of the AGN torus component. In addition to the infrared luminosity, which is computed by integrating the young stellar component's SED from 1 to 1000 μm, these properties include the age and mass of young stars, and the mass of dust which has been produced during the evolution of the starburst. We also report the stellar masses, ages, and the bolometric luminosities (integrating from 0.09 to 1000 μm) of the evolved stellar component. All results are tabulated in Table 5.2, and some are plotted in Fig. 5.4.

5.4.1 Spectral energy distributions

As shown by Rocca-Volmerange et al. (2013, 2015) and by Drouart et al. (2016), the presence of different stellar populations in RG hosts and their strongly accreting supermassive black holes necessitate a fitting approach involving three spectral components, namely the old stellar component, the young stellar component with associated cold dust[4], and the warm AGN torus dust component reemiting the intense AGN radiation. On the one hand, as shown in Fig. 5.2, some of these components can completely dominate the emission in some wavelength domains, as exemplified by the AGN torus emission in the

[4] In the case of 3C 305.1 and 3C 454.1, the young stellar component practically does not contribute to the UV/optical photometry and the *Herschel* photometry could be consistent with the long-wavelength extension of the torus. Hence, in these cases, the sum of merely an old stellar component and an AGN torus component might provide a good representation of the observed SEDs.

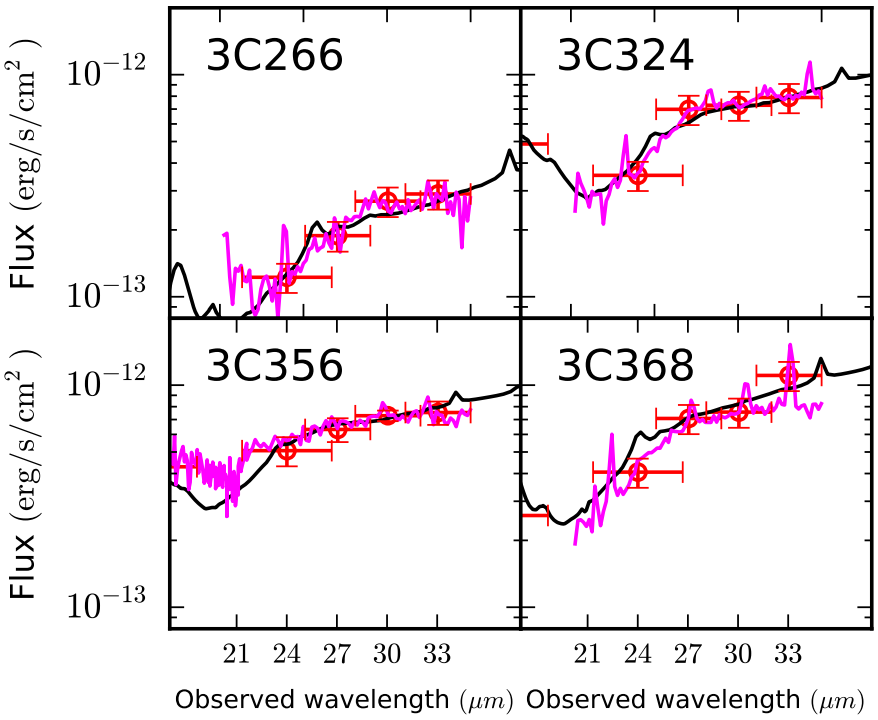

Figure 5.3: Spectral energy distributions (SEDs) in the wavelength domain probed by the *Spitzer* IRS spectra, for the four objects from our sample with such spectra available (Leipski et al. 2010). The IRS spectra and the total SEDs (as presented in Fig. 5.2) are plotted in magenta and black colours, respectively. The photometric data in this wavelength domain (see relevant tables in Appendix) are indicated with red symbols. Note the deep silicate feature in the spectrum of 3C 356 (see text).

MIR. In other wavelength domains, on the other hand, often two (or sometimes all three) components are needed to successfully reproduce the observed SEDs. The AGN-powered torus emission peaks between 20 and 40 μm in the rest-frame MIR, and the young-star-powered dust grain emission peaks between 65 and 90 μm (see Fig. 5.2). With reference to Fig. 5.3, we note that in all cases where *Spitzer* IRS spectra are available, they are exceptionally well reproduced by the torus models, strengthening the view that the disentangling of the torus and cold dust grain emission is done in a robust manner.

The SEDs of the high-z 3CR RGs show a number of characteristic features which we discuss below. The IRS spectra of objects in our work (but also of other 3CR objects from the complete sample, see Leipski et al. 2010) show that PAH features are not prominent (but see Rawlings et al. 2013), suggesting that the MIR emission of the high-z 3CR RGs is completely dominated by the AGN activity (see Fig. 5.3), which is also what is consistently seen in the best-fit models for objects which do not have MIR spectroscopic observations (Fig. 5.2). Moreover, the SEDs of some RGs (e.g., 3C 068.2,

3C 324, 3C 356) show deep silicate features at 9.7 μm rest-frame, and in the case of 3C 356, this silicate feature is also detected in the IRS spectrum shown in Fig. 5.2 and Fig. 5.3 (at an observed wavelength of 20.2 μm). The NIR bump seen in the observed SEDs of some 3CR RGs (e.g., Podigachoski et al. 2015b) is also well reproduced with the Siebenmorgen et al. (2015) library of torus models. In some cases, the strong AGN activity responsible for this NIR bump can outshine the 1 μm peak usually associated with the evolved stellar population in RGs (e.g., 3C 257).

While the adopted three-component approach successfully reproduces the observed SEDs of all RGs, it may not give satisfactory physical results for some particular objects. This mainly concerns the estimated ages of the old stellar components associated with 3C 256, 3C 266, and 3C 368, which as discussed below are estimated to be the youngest throughout the sample. As argued by Best et al. (1998a, for 3C 266 and 3C 368) and Simpson et al. (1999, for 3C 256), these sources are among the ones with the strongest alignment effects[5], and as such we suspect a significant non-stellar contribution to their UV/optical SEDs. However, including yet another spectral component to the radio galaxies' SEDs, or treating some of the UV/optical flux as contributed by direct AGN emission and/or scattered AGN light is outside the scope of this work. Nevertheless, the results obtained for these sources (as indicated below) should be treated with care (see for instance Simpson et al. 1999, for a more detailed analysis of the optical SED of 3C 256). The case for a non-stellar contribution is further discussed in § 5.5.4.

[5] This is the well-known co-spatial extent of the radio and UV/optical emission, resulting from the interaction between the radio-jet and the interstellar matter of the host galaxy in combination with the scattered AGN light (Chambers et al. 1987; McCarthy et al. 1987).

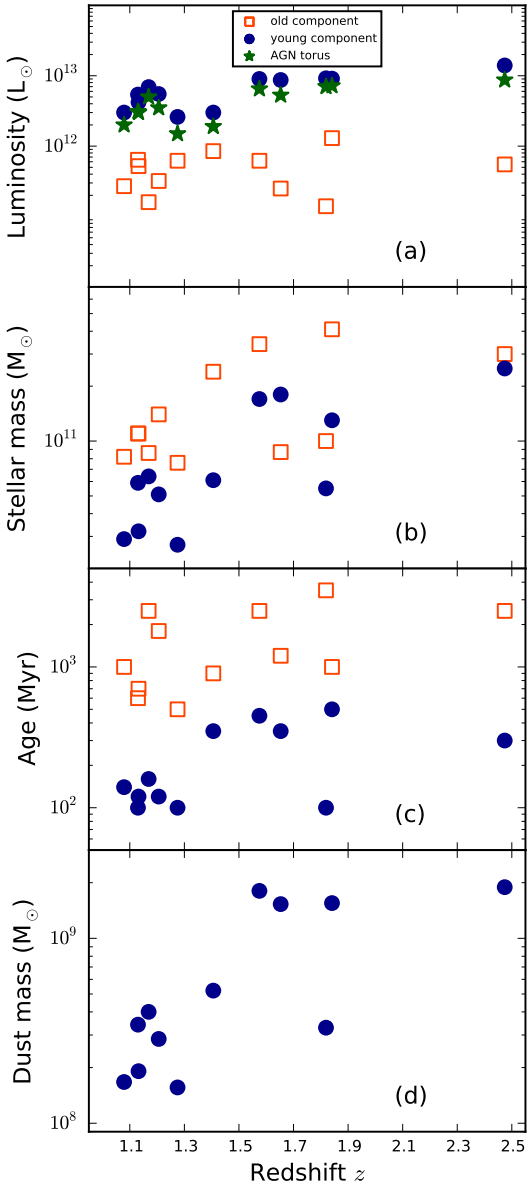

Figure 5.4: Various physical properties of the 3CR radio galaxies obtained using the fitting approach adopted in this work, as a function of redshift. Results for the old and young stellar component are plotted as (orange) empty squares and (blue) circles, respectively, and the AGN-powered torus component is plotted as (green) stars. (a) Luminosities obtained by integrating the relevant best-fit components as described in the text. (b) Masses of the best-fit stellar components. (c) Ages of the best-fit stellar components. (d) Dust mass produced during the evolution of the young stellar component.

Table 5.2: Best-fit physical parameters obtained from spectral energy distribution fitting. The two fits for 3C 256 obtained with and without the UV/optical photometric data (see § 5.5.4), are denoted with superscripts (a) and (b), respectively. Columns represent the following: (1) Object name; (2) bolometric luminosity of the evolved (old) stellar component; (3) infrared (1 to 1000 μm) luminosity of the young (starbursting) stellar component; (4) infrared (1 to 1000 μm) luminosity of the AGN torus component; (5) stellar mass of the old stellar component; (6) stellar mass of the young stellar component; (7) dust mass of the young stellar component; (8) age of the old stellar component; (9) age of the young stellar component; (10) metallicity of the old stellar component; and (11) initial metallicity of the young stellar component.

Name	L^{old}	L^{young}	L^{torus}	$M^{old}_{stellar}$	$M^{young}_{stellar}$	M^{young}_{dust}	Age^{old}	Age^{young}	$Z*^{old}$	$Z*^{young}$
	10^{11} [$L_\odot$]	10^{12} [$L_\odot$]	10^{12} [$L_\odot$]	10^{11} [$M_\odot$]	10^{11} [$M_\odot$]	10^{9} [$M_\odot$]	[Myr]	[Myr]		
3C 068.2	6.2	9.0	6.5	3.4	1.7	1.8	2500	450	0.0187	0.0010
3C 210	1.6	6.9	5.0	0.9	0.6	0.4	2500	160	0.0187	0.0010
3C 256$^{(a)}$	5.9	8.8	6.6	0.1	0.6	0.3	140	120	0.0029	0.0010
3C 256$^{(b)}$	1.4	9.2	7.0	1.0	0.6	0.3	3500	100	0.0192	0.0010
3C 257	5.5	14.0	8.7	3.0	2.5	1.9	2500	300	0.0187	0.0010
3C 266	6.2	2.6	1.5	0.8	0.3	0.2	500	100	0.0114	0.0010
3C 297	8.5	3.0	1.9	2.4	0.6	0.5	900	350	0.0143	0.0010
3C 305.1	5.2	4.2	3.0	1.1	0.3	0.2	700	120	0.0132	0.0010
3C 324	3.2	5.5	3.5	1.4	0.5	0.3	1800	120	0.0174	0.0005
3C 356	2.7	3.0	2.0	0.8	0.3	0.2	1000	140	0.0148	0.0005
3C 368	6.4	5.4	3.1	1.1	0.6	0.3	600	100	0.0124	0.0010
3C 454.1	13.0	9.1	7.2	4.1	1.3	1.6	1000	500	0.0148	0.0005
3C 470	2.5	8.7	5.3	0.9	1.8	1.5	1200	350	0.0155	0.0005

5.4.2 The young stellar component

When modelling the young stellar component (in the following interchangeably referred to as the starburst), we use the extreme case of an instantaneous burst of star formation (Rocca-Volmerange et al. 2013). Adopting such a formalism means that the starbursts in our work are by design in the post-starburst phase (star formation rate is equal to zero), where only the prescriptions from stellar evolution govern, among others, the production of dust grains and the overall SED shape. As expected from the robust *Herschel* detections of the objects in our sample, integrating these SEDs from 1 to 1000 μm yields IR starburst luminosities in excess of 10^{12} $L_{\odot}$ (Fig. 5.4a), which puts them in the domain of ultra-luminous infrared galaxies (ULIRGs, Sanders & Mirabel 1996).

Table 5.2 and Fig. 5.4b show that the starbursts in the host galaxies of our 12 $z > 1$ 3CR objects are massive ones, with estimated stellar masses well above 3×10^{10} $M_{\odot}$ in all cases, and that they amount to $\sim$20 to $\sim$50% of the total stellar mass of the systems. An exception to this trend is the host of 3C 470, wherein the young stellar component contains about 65% of the total stellar mass. Given that 3C 470 is one of the objects with the highest redshifts, and the fact that the young stellar component amounts to about 50% of the total stellar mass of the host of 3C 257 (redshift record-holder in the 3CR sample), these objects could also be supporting the view that their hosts are still going through the process of formation, with a significant amount of stellar mass yet to form. The stellar mass (and consequently the dust mass) of the starburst on average increases when going to high-redshift, which is explained in terms of the selection effect introduced by the *Herschel* detections.

One of the main results from our work is the relatively evolved age of the starburst, which we uniformly find to be greater than 100 Myr across all objects (Fig. 5.4c). While the uncertainty in the age estimates is at best a factor few, the best-fits strongly favour relatively evolved starbursts, allowing – not surprisingly – sufficient time for the process of stellar evolution to generate a dust content of order 10^{8} $M_{\odot}$ (see Fig. 5.4d).

5.4.3 The AGN component

Recall that the high-z 3CR RGs are powerful emitters in the mid-to-far infrared domain (rest-frame wavelengths 5-40 μm Haas et al. 2008; Podigachoski et al. 2015b). The thermal continuum emission at these wavelengths is from the AGN-heated dust in the torus, which clearly dominates over the starburst emission following the diagnostics defined by Brandl et al. (2006). Similarly, considering the emission at 20 μm, which is the wavelength domain used by Drouart et al. (2016) to link the AGN torus to the starburst component, we find that the torus emission is on average an order of magnitude stronger than that of the starburst at this wavelength domain.

Quantifying the different physical parameters associated with the Siebenmorgen et al. (2015) torus library is a challenging task given the small number of broadband MIR photometric data available, therefore we only address the torus luminosity which is calculated from the best-fit model as described above. Nevertheless, when considering all twelve objects studied here, we find that the viewing angles of the tori are always larger than 50° (consistent with these objects being radio galaxies), the cloud volume filling factors

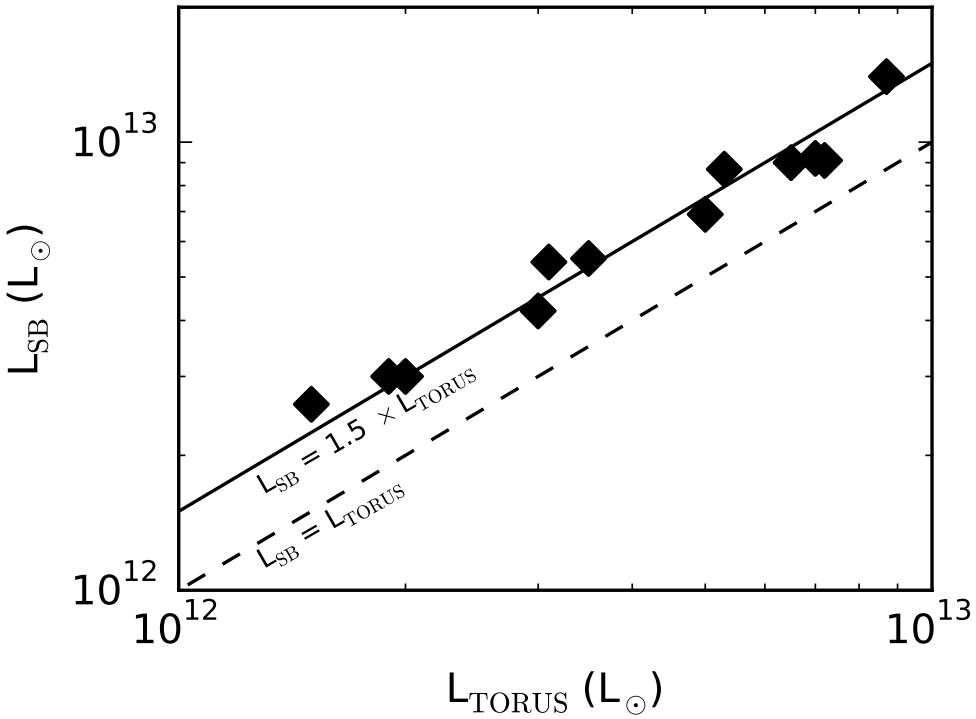

Figure 5.5: Luminosity of the young stellar component as a function of that of the AGN torus component. The dashed and the solid lines indicate the one-to-one and the $L_{SB} = 1.5 \times L_{TORUS}$ lines, respectively.

are generally large (about 80%), and the inner radii of the tori are typically smaller than about 0.25 pc, which means that the sizes of the tori themselves are smaller than about 40 pc (Siebenmorgen et al. 2015). Moreover, the optical depths of clouds avoid the extreme values in the associated parameter space, whereas the optical depths of the tori's disc midplane exhibit no preferential values.

The AGN torus luminosity is plotted in Fig. 5.4a. Like the luminosity of the young stellar component, it ranges between 10^{12} and 10^{13} $L_\odot$, but is systematically lower than that of the young stellar component. Interestingly, the AGN torus luminosity appears to trace well the luminosity of the young stellar component across the entire redshift range, which is better visualized in Fig. 5.5. The observed trend that higher starburst luminosities trace higher torus luminosities, based on the results obtained from the SED-fitting, is an intriguing one, and we return to this point in § 5.5.2.

5.4.4 The evolved stellar component

The template representing the evolved stellar population is in many cases well constrained by the NIR and the shortest wavelength *Spitzer* data, often clearly showing the 1 μm peak

due to evolved stars in the hosts of 3CR sources (Rocca-Volmerange et al. 2013). Hence, one of the more robustly estimated physical properties in this work is the stellar mass of the evolved stellar population. As shown in Fig. 5.4b, this mass is of order 10^{11} $M_{\odot}$ and almost always dominates the stellar mass content of the 3CR host galaxies. While undoubtedly being massive, the 3CR RG hosts appear to be less massive than the most massive elliptical galaxies (10^{12} $M_{\odot}$) corresponding to the brightest luminosity limit of the Hubble K-band diagram (Rocca-Volmerange et al. 2004). Using simple assumptions to subtract the young stellar and non-stellar contributions to only the optical and NIR photometry of the 3CR host galaxies studied in this work, Best et al. (1998a) estimated their stellar masses to be between a factor two to four more massive compared to our estimates. The availability of *Herschel* data which better constrain the contribution of young stars in the optical likely explains our somewhat lower stellar mass estimates compared to those by Best et al. (1998a). A factor of four larger stellar masses for a few of our objects are also reported by Zirm et al. (2003) and Targett et al. (2011), but these numbers are uncertain given that these studies are based exclusively on K-band photometry.

Less constrained is the age of this mature stellar population, which for about half of the objects in this work is in the range of a few billion years (see Fig. 5.4c). The evolved stellar populations of these objects are consistent with being formed at high redshift and evolving passively to the redshift of observation. For the remaining objects, a somewhat lower age (between 0.5 and 1 Gyr) is preferred, and at least some of these are objects for which a contribution from an AGN component cannot be ruled out, so that the sum of an old and a young stellar component is not sufficient for a realistic fit of the observed SED in the UV/optical domain. An extreme example of this is 3C 256, which has both a stellar mass and age of the evolved population an order of magnitude lower than the corresponding properties of the other objects (see details below and discussion by Simpson et al. 1999). Another, more typical, example is 3C 368 (see Appendix for details), which is an object for which the likely AGN contribution leads to lower estimates of the age of the evolved stellar population. For such objects, the age of this stellar population should be treated as an absolute lower limit.

The luminosity of the evolved stellar component is typically above 10^{11} $L_{\odot}$ and is on average an order of magnitude lower than that of either the AGN torus or the young stellar population. Most of the light in the 3CR radio galaxy hosts evidently is absorbed and re-emitted by dust at longer wavelengths.

5.5 Discussion

5.5.1 AGN torus models

Prior to this work, Drouart et al. (2016) analysed the UV-to-submm SEDs of a sample of $1 < z < 4$ radio galaxy hosts using templates based on the PÉGASE.3 models, and the Fritz et al. (2006) library of smooth torus models. We briefly compare the results obtained for two objects, 3C 368 and 3C 470, for which much of the same[6] input data is

[6] The input *Herschel* flux densities are marginally different, whereby we use the photometry by Podigachoski et al. (2015b) and Drouart et al. (2016) used that by Drouart et al. (2014).

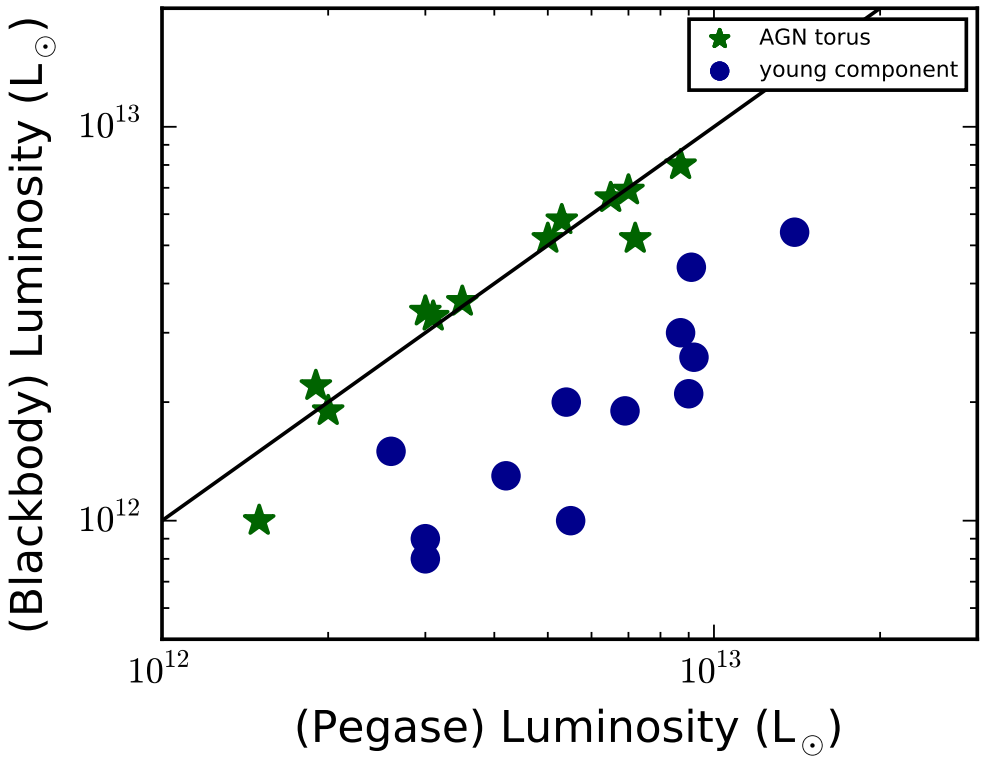

Figure 5.6: Comparison between the luminosities calculated using the Pégase.3 templates and Siebenmorgen et al. (2015) models (this work) and those calculated using a modified blackbody component and Hönig & Kishimoto (2010) models (Podigachoski et al. 2015b). The torus and young stellar components are plotted as (green) stars and (blue) circles, respectively. The one-to-one line is indicated with the solid line.

used in both studies. Considering the best-fit SEDs of these two objects, Drouart et al. (2016) found that the rest-frame wavelength domain between 10 and 50 μm is dominated by the starburst emission, whereas we find that the emission in this domain is largely dominated by the torus emission. This most striking difference is a direct consequence of the adoption of the Siebenmorgen et al. (2015) models in the current work, which results in overall somewhat better fits to the *Herschel* photometry. We refrain from discussing the physical properties of the tori themselves, but we maintain that the Siebenmorgen et al. (2015) models also provide excellent fits to the MIR photometric, and more importantly, spectroscopic observations of the 3CR radio galaxies (Fig. 5.2 and Fig. 5.3). As a result, we find significantly higher torus luminosities and older starbursts, because the strong infrared torus emission associated with the clumpy models allows the peak of the starburst to move to longer wavelengths. The older starbursts in turn emit less extreme-UV radiation, allowing the old stellar components to account for more of the emission in this domain, hence resulting in younger ages compared to those estimated by Drouart

et al. (2016). Evidently, the choice of the AGN torus models can greatly influence the results obtained from SED fitting (but see Feltre et al. 2012). A full comparison between the Drouart et al. (2016) results and those presented here, taking into account the different samples (i.e., different redshift ranges, AGN luminosities, PAH-feature strengths, alignment effect strengths, etc.) is postponed for a future study; how much of the differences can be explained with the different torus models remains to be seen.

Podigachoski et al. (2015b) fitted the infrared SEDs of the complete sample of $z > 1$ 3CR RGs (and quasars) with the sum of a clumpy torus model from Hönig & Kishimoto (2010) and a modified blackbody component. These authors found that in all but two RGs, the AGN torus component has a higher infrared luminosity compared to that of the SF component. We compare these luminosities to those computed in our current work, and present the comparison in Fig. 5.6. On the one hand, the AGN torus luminosities in the two approaches are nearly identical, thereby confirming the reliability of the SED decomposition in the infrared domain. On the other hand, the starburst luminosities are systematically different, such that when using the modified blackbody approach, one underestimates this quantity by a factor of three on average. This difference, however, is easily reconciled when considering that the approach featuring a modified blackbody disregards the additional luminosity emitted by the aromatic features and the continuum radiation at the shorter (few micron) NIR/MIR wavelengths.

5.5.2 The starburst-torus connection

The possible link between the black hole and star formation activity in distant galaxies is largely debated in the literature, with a number of studies involving *Herschel* observations reporting either no/weak or very strong correlation between these two processes (see reviews by Hickox et al. 2014; Lutz 2014). In general, authors who find strong correlations (e.g., Netzer 2009; Bonfield et al. 2011) suggest that such correlations arise naturally given that both processes are being fuelled by the same material, possibly of origins external to the AGN host galaxy.

Figure 5.5 shows a remarkable correlation between the luminosity of the starburst and that of the AGN torus. Both luminosities roughly cover one order of magnitude, which is also the range for the radio luminosity shown in Fig. 5.1. As indicated by the solid line in the figure, in all cases the starburst luminosity exceeds that of the AGN torus by a factor of 1.5, with small scatter. The strong correlation and the constant ratio between the luminosities suggest that the two processes know about and possibly influence each other. One possible way in which this physical link could be established is if part of the dust produced in the current starburst ends up in the AGN torus, so that it provides extra material for intercepting the incoming radiation from the accretion disk. A consequence of this interpretation is that for objects of similar intrinsic AGN luminosity, like the 3CR RGs in our sample, the torus luminosity increases with increasing the starburst dust mass, in line with what is shown in Fig. 5.7. For this interpretation to hold, the starbursts reported in this work should ideally take place in the circumnuclear regions, i.e., on scales <1 kpc, which could observationally be tested making use of the superb capabilities of the ALMA observatory.

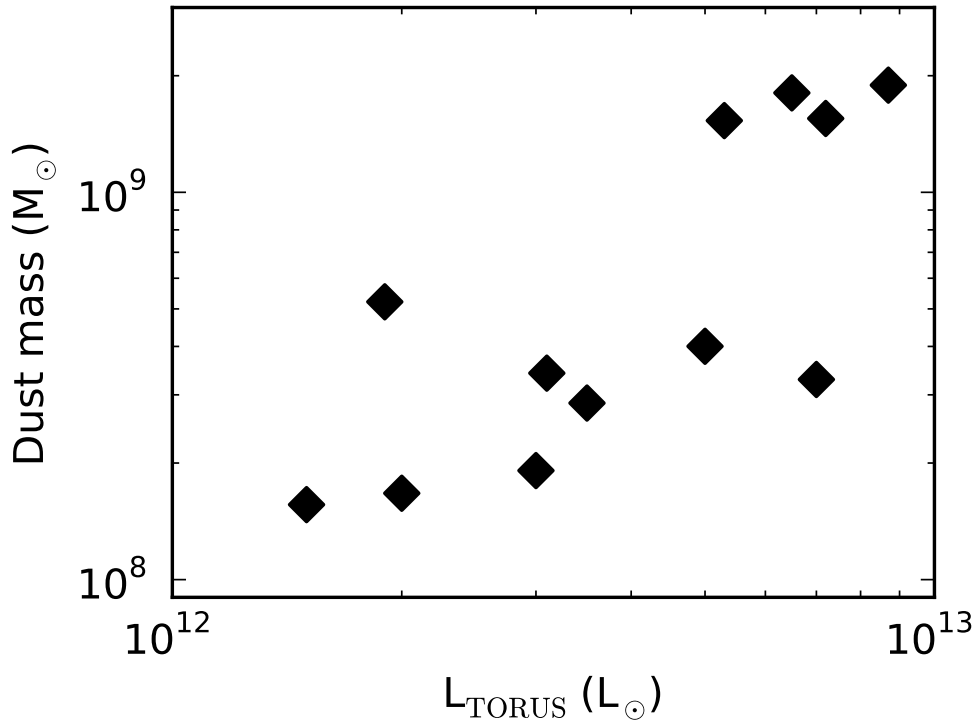

Figure 5.7: Dust mass of the starburst component versus the infrared (1-1000μm) luminosity of the AGN torus component.

While the strong L_{SB}-L_{TORUS} correlation clearly holds for the twelve RGs of the present work[7], it likely breaks down for the *Herschel*-undetected $z > 1$ 3CR RGs. Recall that all RGs from the complete high-z 3CR sample are detected with all instruments on *Spitzer* (Haas et al. 2008), while only the most starbursting ones (close to 40%) are detected at the longest *Herschel* wavelengths (Podigachoski et al. 2015b) such that their young stellar components are as luminous as the AGN-tori. This means that powerful starbursts are associated with luminous torus components, but not the other way around. Hence, the correlation presented in Fig. 5.5 is likely the envelope of the L_{SB}-L_{TORUS} relation, tracing the redshift-dependent luminosity, and the *Herschel*-undetected objects, with luminosities significantly below the ULIRG domain, likely populate regions well below this envelope.

5.5.3 Age effect

High-resolution radio imaging provides a unique opportunity of measuring the lobe-to-lobe distance in RGs. Assuming a typical advance rate of the radio jet (10-20% of the

[7] In the case of 3C 305.1 and 3C 454.1, whose observed spectral energy distributions might also be consistent with a sum of an evolved stellar and torus component, the correlation as presented would not necessarily hold.

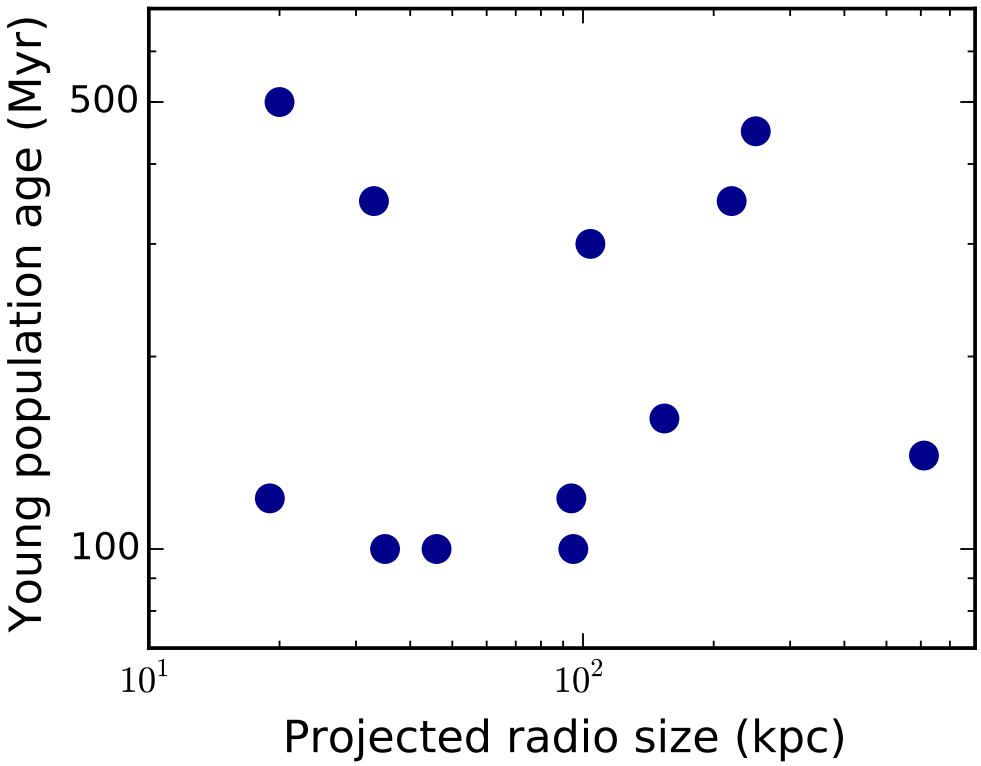

Figure 5.8: Age of the young stellar population obtained from PÉGASE.3 as a function of the projected size of the radio source. The latter is the distance between the radio-lobes on either side of the AGN host, and is often used as a proxy for the age (duration) of the current AGN episode.

speed of light) and limited projection effects, such a measurement can be treated as a proxy for the duration of the current AGN episode. The radio size and the age of the young stellar population have been used in the literature to ascertain whether the triggering of the star formation and AGN activity are related to one another, and perhaps linked in an evolutionary scenario (see e.g., Tadhunter et al. 2011, and references therein).

Figure 5.8 shows the age of the young stellar population as a function of the projected size of the central radio source. No clear trend is evident, i.e., both small and large radio sources are found in hosts of both younger (100 Myrs) and somewhat older (300 - 500 Myr) young stellar populations. One interpretation of this result is that the onsets of the starburst and AGN activity do not follow a unique scenario, in line with what has been found by Tadhunter et al. (2011) for nearby RGs. However, given the relatively evolved starbursts witnessed in our 3CR RG hosts, if both activities are triggered within a merger event (e.g., Mihos & Hernquist 1996), for which evidence was recently presented by Chiaberge et al. (2015), it appears more likely that the starbursts precede or are at

least concurrent with the AGN episode. This interpretation, however, remains uncertain given the errors in the starburst age estimates. UV/optical spectra could in principle provide better age estimates, however the strong AGN activity and pronounced alignment effect in the high-z 3CR population will likely complicate such age estimates. Based on the *Herschel* detection rates of their complete $z > 1$ 3CR sample of RGs and quasars, Podigachoski et al. (2015b) speculated that the starburst activity in the subgalactic-sized (<30 kpc) radio sources (e.g., O'Dea 2016) may be triggered by the jet activity. The relatively evolved starbursts we find in the current work appear incompatible with this scenario of positive feedback, and the incidence (or lack) of feedback remains to be verified using the superb ALMA capabilities.

5.5.4 Caveat: apertures and non-stellar UV/optical continua

Simultaneously studying the properties of the stellar populations and the AGN-powered emission of statistically important samples of RGs requires the availability of good quality photometric data covering much of the electromagnetic spectrum. This necessarily leads to using data from instruments with significantly different spatial resolutions, as for example in the case of the *HST* and *Herschel* (SPIRE) data, which means that different physical regions are explored particularly in high-redshift objects like those studied in this work. Despite the fact that the apertures used for measuring the fluxes used in our work are often different, the effects on the obtained results are expected to be minimal, given that the apertures are often big enough to include most of the light from the AGN host galaxy.

Powerful RGs often show evidence for some non-stellar contribution to their UV/optical continuum. This may be either due to AGN-powered nebular continuum (e.g., Dickson et al. 1995), and/or light scattered off dust particles present in the polar regions (e.g., di Serego Alighieri et al. 1994). The fact that the non-stellar contribution is not addressed here is, arguably, the main limitation of the current work. When fitting the UV/optical SEDs of high-z RGs, Best et al. (1998a) approximated the total contribution from both processes with a power-law with a fixed spectral index, however, constraining the contribution from each process (and hence the power-law index) is not possible with the UV/optical data available for our work. However, based on the alignment effect (as discussed in § 5.4.1), we expect a non-stellar contribution to the SEDs of only a few RGs studied (i.e., 3C 256, 3C 266, and 3C 368), and in those cases, the results obtained should be treated with care (see also § 5.4.4).

The most striking example in which the spectral shape of the UV/optical SED is clearly of non-stellar origin is 3C 256 (Simpson et al. 1999). A simple way to examine how the resulting physical properties are influenced by the presence of non-stellar contribution in 3C 256's host is to repeat the fit excluding the UV/optical photometric data (see Fig. 5.9). Comparing the two fits, the clear difference is in the region covered by the *Spitzer* IRAC bands, and without the requirement to fit the UV/optical points, the evolved stellar component contributes with equal weight compared to the young component in this domain. Furthermore, the extreme UV emission in the revised fit is dominated by the young stellar component. Not surprisingly, major differences are found in the estimated properties of the evolved stellar populations in the two scenarios: the

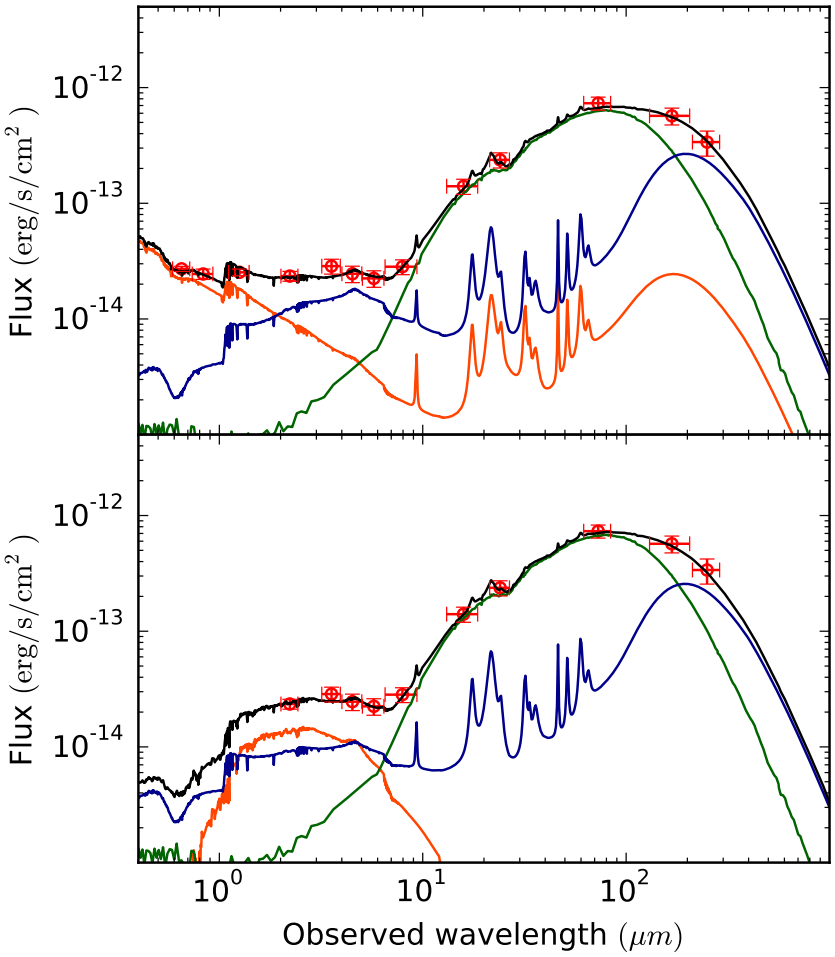

Figure 5.9: Fitting the spectral energy distribution of 3C 256 using all available photometric data listed in Table 5.5 (upper panel) and only data beyond K-band (lower panel). The lines and the symbols are identical as in Fig. 5.2. While the physical properties estimated from the AGN and young stellar component are similar in both scenarios, those from the evolved stellar component are strikingly different (see text for more details), and clearly incorrect in the upper SED fit.

stellar mass goes up by a factor of ten, and the age increases from 140 to 3000 Myr (see Table 5.2). Given that Fig. 5.9 likely traces the extreme cases of old and young stellar component dominance in the UV domain, the results obtained for the old stellar component should be treated as limits. However, the AGN torus luminosity and the properties of the young stellar component (mass, age, luminosity, metallicity) remain within 10% in both cases, which shows that the results obtained from the longer-wavelength part of the SED are fairly robust and not particularly sensitive on the possible presence of non-stellar contribution in the shortest wavelengths.

5.5.5 Concluding remarks

We conclude the discussion section by presenting a number of possibilities for further exploration and verification of the results obtained in this work. One such possibility is to relax the extreme case of instantaneous starburst, and to investigate more plausible scenarios with somewhat longer duration of star formation activity. Another possibility is to extend our limited redshift coverage and break the redshift degeneracy by applying our approach, including the same torus models, to a larger compilation of objects consisting of the high-z ($1 < z < 4$) RGs from the study by Drouart et al. (2016) and the low-z ones ($0.5 < z < 1$) addressed by Westhues et al. (2016). In such a study, two-component fits (evolved young population and a torus model) could also be considered for objects in which the starburst contributes only at the longest *Herschel* bands. Such a systematic study could also shed more light on the recently proposed idea of SMBH growth through accretion of supernova remnants accumulated along the star formation histories of RG hosts (Rocca-Volmerange et al. 2015).

5.6 Conclusions

We studied the ultraviolet-to-submillimetre broad-band spectral energy distributions (SEDs) of a sample of twelve *Herschel*-detected 3CR radio galaxies covering the redshift range $1 < z < 2.5$, using stellar templates produced by the evolutionary code Pégase.3 and state-of-the-art templates describing the emission from AGN-heated dust in the torus. We find that the observed photometric SEDs, and in four objects also the *Spitzer* spectra, are in most cases well represented by a three-component model, which in addition to strong AGN torus emission includes both an evolved and massive stellar component (1 Gyr or older) and a starburst, confirming previous studies in the literature. The best-fit SEDs yield relatively evolved (∼100 Myr or older) extremely massive starbursts which contain 20-50% of the stellar mass of the systems, with infrared luminosities systematically larger than those of the AGN torus component. The observed correlation between these two luminosities is intriguing, but remains to be confirmed with a more robust analysis based on statistically larger samples of radio galaxy hosts.

Acknowledgements
This research was financially supported by Ammodo, through a Van Gogh travel grant. We thank Marco Chiaberge for kindly providing data prior to publication, and the expert referee for insightful comments and suggestions which improved the clarity of the paper. P.P. acknowledges the Nederlandse Organisatie voor Wetenschappelijk Onderzoek (NWO) for a Ph.D. fellowship, and the Leids Kerkhoven-Bosscha Fonds (LKBF) for a generous travel grant to the Institut d'Astrophysique de Paris.

Appendix 5.A Notes on individual spectral energy distributions

3C 210 — 3C 210 has only two strong *Herschel* detections, however its redshift of $z = 1.17$ ensures that the PACS 160 μm band probes emission beyond 70 μm, hence it is included in our sample.

Table 5.3: Table of photometric data used to fit the spectral energy distribution of 3C 068.2. The UV/optical data presented are emission-line corrected, as explained in the relevant references provided. Aperture sized used for the photometry can also be found in the same references. References: (1) Best et al. (1997), (2) Haas et al. (2008), (3) Podigachoski et al. (2015b).

Band	Wavelength [μm]	Flux density [μJy]	Ref.
HSTF785LP	0.9	7.9±0.9	(1)
UKIRTJ	1.2	35.0±5.8	(1)
UKIRTK	2.2	65.0±7.2	(1)
IRAC1	3.6	105±16	(2)
IRAC2	4.5	129±19	(2)
IRAC3	5.8	137±21	(2)
IRAC4	8.0	112±17	(2)
IRS	16	1340±201	(2)
MIPS1	24	1170±176	(2)
PACS70	70	27500±2600	(3)
PACS160	160	39600±5900	(3)
SPIRE250	250	42000±7200	(3)
SPIRE350	350	38700±7000	(3)
SPIRE500	500	29000±7200	(3)

Table 5.4: Same as Table 5.3, but for 3C 210. References: (1) Chiaberge et al. (2015), (2) Haas et al. (2008), (3) Podigachoski et al. (2015b).

Band	Wavelength [μm]	Flux density [μJy]	Ref.
HST3F606W	0.6	7.1±0.2	(1)
HST3F140W	1.4	44.1±0.2	(1)
IRAC1	3.6	256±38	(2)
IRAC2	4.5	336±50	(2)
IRAC3	5.8	489±73	(2)
IRAC4	8.0	1090±164	(2)
IRS	16	3410±512	(2)
MIPS1	24	4430±665	(2)
PACS70	70	31600±2400	(3)
PACS160	160	56000±4000	(3)

Table 5.5: Same as Table 5.3, but for 3C 256. References: (1) Simpson et al. (1999), (2) Haas et al. (2008), (3) Podigachoski et al. (2015b).

Band	Wavelength [μm]	Flux density [μJy]	Ref.
CFHTR	0.7	5.9±0.3	(1)
CFHTI	0.8	6.8±0.7	(1)
NIRCJ	1.2	10.6±0.7	(1)
NIRCK	2.2	17.4±1.7	(1)
IRAC1	3.6	34±5	(2)
IRAC2	4.5	37±6	(2)
IRAC3	5.8	43±7	(2)
IRAC4	8.0	75±11	(2)
IRS	16	743±111	(2)
MIPS1	24	1900±285	(2)
PACS70	70	17800±2300	(3)
PACS160	160	31900±5300	(3)
SPIRE250	250	28200±6900	(3)

3C 256 — This is one of the objects in which the alignment effect in the UV/optical is particularly pronounced (see for example Simpson et al. 1999). For a complete discussion on this issue, we refer the reader to § 5.5.4, and in particular to Fig. 5.9. Note that by excluding the UV/optical photometric data in the revised fit in Fig. 5.9, 3C 256 technically no longer satisfies the selection criteria explained in § 5.2.

3C 257 — This is the highest redshift ($z = 2.47$) object in both our sample and in the complete $z > 1$ 3CR radio-loud sample.

3C 266 — For this object, Inskip et al. (2006) computed the UV/optical and near-infrared photometry using apertures of 4″in diameter (as opposed to that of 9″used by Best et al. 1997). We applied our fitting approach using the Inskip et al. data as input, and found that the estimated physical parameters remain practically the same (within 10%). This is one of the four objects in the redshift range $1 < z < 1.4$ for which *Spitzer* IRS spectra are available.

3C 305.1 — The UV-to-submm spectral energy distribution of this object could also be well represented with a two-component model, this being the sum of an evolved stellar component and the AGN torus component. In this case, the results for the evolved component would remain unchanged, whereas the luminosity of the torus would increase.

3C 324 — This is one of the four objects in the redshift range $1 < z < 1.4$ for which *Spitzer* IRS spectra are available.

3C 356 — 3C 356 has only two strong *Herschel* detections, however its redshift of

Table 5.6: Same as Table 5.3, but for 3C 257. References: (1) Chiaberge et al. (2015), (2) Haas et al. (2008), (3) Podigachoski et al. (2015b), (4) Archibald et al. (2001).

Band	Wavelength [μm]	Flux density [μJy]	Ref.
HST3F606W	0.6	0.6±0.1	(1)
HST3F140W	1.4	10.0±0.2	(1)
IRAC1	3.6	85±13	(2)
IRAC2	4.5	111±17	(2)
IRAC3	5.8	194±29	(2)
IRAC4	8.0	322±48	(2)
MIPS1	24	1360±204	(2)
PACS70	70	8100±1000	(3)
PACS160	160	15600±2500	(3)
SPIRE250	250	33100±4700	(3)
SPIRE350	350	31800±5500	(3)
SPIRE500	500	32300±8600	(3)
SCUBA850	850	5400±950	(4)

Table 5.7: Same as Table 5.3, but for 3C 266. References: (1) Best et al. (1997), (2) Haas et al. (2008), (3) Podigachoski et al. (2015b). The flux densities measured from the *Spitzer* IRS spectrum in the artificial broadband filters centred at 27, 30, and 33 μm are 1.7±0.3, 2.7±0.4, and 3.2±0.5 mJy, respectively.

Band	Wavelength [μm]	Flux density [μJy]	Ref.
HSTF555W	0.5	7.9±0.5	(1)
HSTF702W	0.7	11.6±0.8	(1)
HSTF814W	0.8	15.7±0.5	(1)
UKIRTK	2.2	56.1±4.7	(1)
IRAC1	3.6	68±10	(2)
IRAC2	4.5	73±11	(2)
IRAC3	5.8	45±7	(2)
IRAC4	8.0	102±15	(2)
IRS	16	370±56	(2)
MIPS1	24	980±147	(2)
PACS70	70	7600±2400	(3)
PACS160	160	29400±4100	(3)
SPIRE250	250	19500±5600	(3)

Table 5.8: Same as Table 5.3, but for 3C 297. References: (1) Chiaberge et al. (2015), (2) Haas et al. (2008), (3) Podigachoski et al. (2015b).

Band	Wavelength [μm]	Flux density [μJy]	Ref.
HST3F606W	0.6	6.6±0.2	(1)
HST3F140W	1.4	64.3±0.2	(1)
IRAC1	3.6	119±18	(2)
IRAC2	4.5	126±19	(2)
IRAC3	5.8	122±18	(2)
IRAC4	8.0	121±18	(2)
MIPS1	24	432±65	(2)
PACS70	70	12600±1200	(3)
PACS160	160	15400±2400	(3)
SPIRE250	250	24500±4300	(3)

Table 5.9: Same as Table 5.3, but for 3C 305.1. References: (1) Chiaberge et al. (2015), (2) Haas et al. (2008), (3) Podigachoski et al. (2015b).

Band	Wavelength [μm]	Flux density [μJy]	Ref.
HST3F606W	0.6	10.7±0.2	(1)
HST3F140W	1.4	60.3±0.2	(1)
IRAC1	3.6	181±27	(2)
IRAC2	4.5	282±42	(2)
IRAC3	5.8	495±74	(2)
IRAC4	8.0	972±146	(2)
IRS	16	2410±362	(2)
MIPS1	24	2490±374	(2)
PACS70	70	24000±2300	(3)
PACS160	160	40400±4300	(3)
SPIRE250	250	34900±6000	(3)

Table 5.10: Same as Table 5.3, but for 3C 324. References: (1) Chiaberge et al. (2015), (2) Best et al. (1997), (3) Haas et al. (2008), (4) Podigachoski et al. (2015b), (5) Best et al. (1998b). The flux densities measured from the *Spitzer* IRS spectrum in the artificial broadband filters centred at 27, 30, and 33 μm are 6.3±1.0, 7.3±1.1, and 8.7±1.3 mJy, respectively.

Band	Wavelength [μm]	Flux density [μJy]	Ref.
HST3F606W	0.6	4.7±0.2	(1)
HSTF702W	0.7	7.8±0.6	(2)
HSTF791W	0.8	12.5±1.2	(2)
UKIRTJ	1.2	57.6±5.8	(2)
HST3F140W	1.4	48.3±0.2	(1)
UKIRTK	2.2	103.0±6.6	(2)
IRAC1	3.6	165±25	(3)
IRAC2	4.5	160±24	(3)
IRAC3	5.8	178±27	(3)
IRAC4	8.0	450±68	(3)
IRS	16	2580±387	(3)
MIPS1	24	2820±423	(3)
PACS70	70	23500±2300	(4)
PACS160	160	31700±5600	(4)
SPIRE250	250	21000±6200	(4)
SCUBA850	850	3010±720	(5)

$z = 1.08$ ensures that the PACS 160 μm band probes emission beyond 70 μm, hence it is included in our sample. This is one of the four objects in the redshift range $1 < z < 1.4$ for which *Spitzer* IRS spectra are available.

3C 368 — The optical/UV spectral shape requiring a relatively low age of the evolved stellar population, together with the shape of the NIR SED traced by the shorter *Spitzer* bands suggest that some AGN contribution is likely present in the optical photometry of this object. This might be consistent with Best et al. (1998a), who argued that 3C 368 has the strongest alignment effect among the ones studied in their sample, so that the non-stellar contribution to the K-band photometry is about 30%. This is one of the four objects in the redshift range $1 < z < 1.4$ for which *Spitzer* IRS spectra are available.

3C 454.1 — The UV-to-submm spectral energy distribution of this object might also be well represented with a two-component model, this being the sum of an evolved stellar component and the AGN torus component. In this case, the results for the evolved component would remain unchanged, whereas the luminosity of the torus would increase.

3C 470 — It is the only object in our sample, in which the stellar mass of the young stellar component is significantly larger than that of the evolved stellar component.

Table 5.11: Same as Table 5.3, but for 3C 356. References: (1) Chiaberge et al. (2015), (2) Best et al. (1997), (3) Haas et al. (2008), (4) Podigachoski et al. (2015b). The flux densities measured from the *Spitzer* IRS spectrum in the artificial broadband filters centred at 27, 30, and 33 μm are 5.7±0.7, 7.3±0.4, and 8.3±1.0 mJy, respectively.

Band	Wavelength [μm]	Flux density [μJy]	Ref.
HST3F606W	0.6	5.6±0.2	(1)
HSTF622W	0.6	7.4±0.6	(2)
HSTF814W	0.8	13.1±1.0	(2)
HST3F140W	1.4	45.3±0.2	(1)
UKIRTK	2.2	64.4±3.6	(2)
IRAC1	3.6	108±16	(3)
IRAC2	4.5	110±16	(3)
IRAC3	5.8	122±18	(3)
IRAC4	8.0	434±65	(3)
IRS	16	2270±341	(3)
MIPS1	24	4060±609	(3)
PACS70	70	11600±2500	(4)
PACS160	160	19700±4900	(4)

Table 5.12: Same as Table 5.3, but for 3C 368. References: (1) Best et al. (1997), (2) Haas et al. (2008), (3) Podigachoski et al. (2015b), (4) Archibald et al. (2001). The flux densities measured from the *Spitzer* IRS spectrum in the artificial broadband filters centred at 27, 30, and 33 μm are 6.4±1.0, 7.6±1.1 and 12.2±1.8 mJy, respectively.

Band	Wavelength [μm]	Flux density [μJy]	Ref.
HSTF702W	0.7	21.7±2.6	(1)
HSTF791W	0.8	27.5±4.1	(1)
UKIRTJ	1.2	66.1±9.1	(1)
UKIRTK	2.2	99.3±13.7	(1)
IRAC1	3.6	126±19	(2)
IRAC2	4.5	112±17	(2)
IRAC3	5.8	112±17	(2)
IRAC4	8.0	210±32	(2)
IRS	16	1370±206	(2)
MIPS1	24	3250±488	(2)
PACS70	70	29900±2000	(3)
PACS160	160	61500±4800	(3)
SPIRE250	250	44400±7400	(3)
SPIRE350	350	23800±6200	(3)
SCUBA850	850	4080±1080	(4)

Table 5.13: Same as Table 5.3, but for 3C 454.1. References: (1) Chiaberge et al. (2015), (2) Haas et al. (2008), (3) Podigachoski et al. (2015b).

Band	Wavelength [μm]	Flux density [μJy]	Ref.
HST3F606W	0.6	3.6±0.4	(1)
HST3F140W	1.4	53.5±0.2	(1)
IRAC1	3.6	77±12	(2)
IRAC2	4.5	76±11	(2)
IRAC3	5.8	112±17	(2)
IRAC4	8.0	135±20	(2)
IRS	16	612±92	(2)
MIPS1	24	1500±225	(2)
PACS70	70	13700±2500	(3)
PACS160	160	37000±4700	(3)
SPIRE250	250	50200±8700	(3)
SPIRE350	350	26700±10400	(3)

Table 5.14: Same as Table 5.3, but for 3C 470. References: (1) Best et al. (1997), (2) Haas et al. (2008), (3) Podigachoski et al. (2015b), (4) Archibald et al. (2001).

Band	Wavelength [μm]	Flux density [μJy]	Ref.
HSTF785LP	0.9	3.9±1.4	(1)
UKIRTK	2.2	39.9±5.5	(1)
IRAC1	3.6	50±7	(2)
IRAC2	4.5	75±11	(2)
IRAC3	5.8	72±11	(2)
IRAC4	8.0	266±40	(2)
IRS	16	1510±227	(2)
MIPS1	24	2650±398	(2)
PACS70	70	16000±2700	(3)
PACS160	160	29300±5100	(3)
SPIRE250	250	48000±6500	(3)
SPIRE350	350	36300±5200	(3)
SCUBA850	850	5640±1080	(4)